Supplementary Material for

How the Cucumber Tendril Coils and Overwinds

Sharon J. Gerbode, Joshua R. Puzey, Andrew G. McCormick, L. Mahadevan*

*To whom correspondence should be addressed. E-mail: lm@seas.harvard.edu

Published 31 August 2012, *Science* **337**, 1087 (2012)
DOI: 10.1126/science.1223304

This PDF file includes:

Other Supplementary Material for this manuscript includes the following:
(available at www.sciencemag.org/cgi/content/full/337/6098/1087/DC1)

Movies S1 to S11

Section 1: Materials and Methods

Description of growth conditions

All plants were grown in the Department of Organismic and Evolutionary Biology greenhouses at Harvard University in long day conditions of 16 hour light/8 hour dark at a constant temperature of approximately 25°C.

Microscopy

A Zeiss AxioImager Z2 (Harvard Imaging Center) fitted with a Zeiss AxioCam Mrc digital camera was used for capturing darkfield and UV images of tendril cross sections. Fiber ribbons were imaged with an Insight Spot camera mounted on a Leica Wild M10 dissecting scope. Color images of tendrils, models, and fiber ribbons were taken with a Nikon D40x.

Fiber ribbon extraction

To extract fiber ribbons from whole tendrils, a solution of 2% Driselase (by weight) in phosphate buffered saline (PBS) was prepared. Since Driselase does not go completely into solution in PBS, the mixture was vortexed vigorously and then allowed to sit for 30 minutes. A fresh tendril was submerged in the Driselase supernatant and stored at 37°C overnight. After soaking overnight, the tendril was removed and briefly rinsed in fresh PBS. Forceps were used to gently slide the broken-down epidermal cells off of the fiber ribbon.

Physical model construction

Composite bilayer strips were constructed from prestrained silicone rubber in a three step process. First, a wide silicone rubber sheet was stretched along one axis to approximately 1.75 times its initial length (strain = 1.75), and was held clamped at this length. Second, another silicone layer consisting of Dow-Corning 732 multipurpose silicone sealant was added to the

stretched sheet along the strained axis, far from the edges of the sheet. Upon curing, the two layers were permanently bonded, creating a composite prestrained structure. In the final step, strips approximately 8 mm wide were cut along the stretched direction, and then the ends of the strips were released, allowing the composite material to relax to its equilibrium shape, with intrinsic curvature set by the relative strain, thickness, and stiffness of the two layers.

Force measurement apparatus

Tendrils were clamped at one end to a translation stage (Newport 426 crossed-roller bearing linear stage, with a Newport universal controller, model ESP 300) and clamped at the other end to a full bridge thin beam load cell (Omega LCL-113G) connected via a digital transmitter (Omegabus D1521) to RS-232. Custom LabVIEW software was used to move the translation stage in steps of 0.1 mm, measure force with the load cell, and simultaneously image the tendril with a digital ccd camera (Allied Vision Technologies Marlin) to monitor overwinding or unwinding behavior. Since both ends of the tendril were clamped, the ends were prevented from rotating during extension.

Numerical simulations of helical rods

As described in the main text, tendrils are a composite of a soft, fleshy bulk and a very stiff fiber ribbon. Here, we do not analyze the detailed mechanics of the composite tendril, and instead focus on a simple model that allows us to uncover the mechanical response of the tendril using a 1-dimensional equivalent filament with a naturally helical shape due to the asymmetric shrinkage of the fiber ribbon. This approximation allows us to capture the mechanics of the tendril on length scales that are large compared to its radius, as well as its bending, twisting, shear and extensional stiffness which we assume to be uniform along the filament. As the filament deforms in response to boundary or body forces, there is an elastic potential energy associated

with bending, twisting, shear and extensional deformations as well as a kinetic energy associated with the velocity of the rod (although the effect of inertia is irrelevant in our problem, as expected). Geometrically, the deformed rod is described by a curvature vector $\mathbf{k} - \mathbf{k}_0$ which describes how a material frame attached to a cross-section bends and twists relative to its intrinsic curvature $\mathbf{k}_0$, a local shear vector $\sigma - \sigma_0$ that describes the axial extension and planar shear relative to the intrinsic shear σ_0, a local centerline velocity $\mathbf{v}$, and a local angular velocity $\mathbf{w}$. The total energy of the rod is then given by (*28*):

$$\begin{aligned} E_{bend/twist} &= \frac{1}{2}\int_0^S (\mathbf{k}-\mathbf{k}_0)^T \mathbf{B}(\mathbf{k}-\mathbf{k}_0)\, ds \\ E_{stretch/shear} &= \frac{1}{2}\int_0^S (\sigma-\sigma_0)^T \mathbf{G}(\sigma-\sigma_0)\, ds \\ E_{translate} &= \frac{1}{2}\int_0^S \rho \mathbf{v}^T\mathbf{v}\, ds \\ E_{rotate} &= \frac{1}{2}\int_0^S \mathbf{w}^T\mathbf{I}\mathbf{w}\, ds \end{aligned} \tag{1}$$

where we have assumed a simple quadratic form for the potential energy terms and where S is the total length of the rod, $\mathbf{B}$ is the local bending/twisting stiffness matrix, $\mathbf{G}$ is the local shearing/stretching stiffness matrix, ρ is the mass per unit length, and $\mathbf{I}$ is the moment of inertia of the cross-section. Our model used is similar, but not identical, to that described in (*27*); in particular, we differ by accounting for the role of both extensional and shear deformations; a complete description of this generalized theory will follow in a future paper. Although the Hamiltonian above is quadratic, the resulting Euler-Lagrange equations are nonlinear owing to the fact that we make no approximations in describing the curvature and torsion of the centerline of the filament, both of which can be relatively large.

To make progress in solving for the shape of the composite filament, we discretize the energy 1, describing the rod's centerline by n+1 vertices connected by n edges, so that we can derive a discrete set of equations of motion for the vertices by using standard techniques from

the calculus of variations. The equations of motion are then integrated using a semi-implicit Euler method, and the boundary conditions are explicitly applied at each time step. Since our experiments were carried out quasi-statically, the effects of inertia were negligible so that we used an over damped version of the equations of motion, as $\rho v^2/Bk^2 \ll 1, I\omega^2/Bk^2 \ll 1$. Furthermore, our filaments were very stiff in shear and extension so that we took $B/\sigma L^2 \ll 1$. To mimic the aging of the tendril, we varied the ratio of the bending to twisting stiffness.

The mechanical response of a tendril with a perversion may be understood by first constructing one. We clamp a naturally curved right handed helix to its mirror image, a left handed helix; the internal clamping point chosen to have no intrinsic curvature. Next, the ends of the rod were clamped (and unable to rotate) to supports that were pulled apart at a constant, quasi-static velocity. This system has a natural symmetry about the perversion that effectively reduces the problem into deforming a single helix with the mid-point being free to rotate but unable to translate in the axial direction. Thus, the mathematical significance of a perversion is that it changes the effective boundary conditions for each of its constituent helices by allowing them to rotate about their point of chiral asymmetry and accommodate the applied deformations by either overwinding or or unwinding depending on the ratio of the bending to twisting stiffness of the filament.

Dimensionless force-extension curves

To compare between tendrils of different lengths and stiffnesses, and also to enable comparison with our numerical simulations, we scaled the measured force-extension curves by defining the scaled displacement $\Delta l = (L - L_0)/S$ as the instantaneous axial length L of the tendril relative to its relaxed axial length L_0, divided by its total arc length S. Additionally, we defined the dimensionless force $\tilde{F}$ as the force F measured for any given tendril or numerical simulation, divided by an arbitrary force constant F_0. We chose F_0 to be the force required to initially

deform the perverted segment of the young tendril (dotted red curve in Fig. 3A) by a unit scaled displacement, i.e. $F_0 = \partial F/\partial(\Delta l)$ of the force-extension curve of the perverted segment of the young tendril.

Section 2: Theory

Intrinsic curvature of a prestrained bilayer ribbon

In cucumber tendrils, we observe that coiling occurs as a result of the morphosis of the fiber ribbon, a bilayer strip of long cells that extends along the entire length of the tendril. As one layer of the ribbon shrinks relative to the other, the composite ribbon develops intrinsic curvature. We have experimentally mimicked this process using prestrained bilayer rubber models as described in the manuscript. Here we give expressions for the intrinsic curvature k_0 of a bilayer rectangular cross-section ribbon with prestrain induced by the differential shrinkage of the constituent strips using expressions derived for the curvature of a heated bimetallic strip that bends due to the differential expansion of its constituent elements by Timoshenko (*29*), which we include here for completeness.

Consider two elastic ribbons of equal width t and heights h_1 (lower red in Fig. S3) and h_2 (upper blue in Fig. S3) that are combined to make a bilayer ribbon. The lower layer has Young's modulus E_1 while the upper layer has Young's modulus E_2. The lower layer is first stretched to a strain value of ϵ_1^* and is held in tension. The upper layer is not stretched, so that $\epsilon_2^* = 0$, and is permanently bonded to the lower layer. Then, when tension is released on the bonded bilayer ribbon, it relaxes to its equilibrium configuration with strains ϵ_1 and ϵ_2 and curvature k_0. The value of the intrinsic curvature k_0 is determined by the relative strain, Young's moduli, and heights of each layer. Both force and torque are balanced in the bilayer ribbon when it is left

free, so that

$$\begin{aligned} F_1 &= F_2 \quad \text{(Force balance)} \\ F_1 h_1/2 + F_2 h_2/2 &= k_0(E_1 I_1 + E_2 I_2) \quad \text{(Torque balance)} \end{aligned}$$

where $I_1 = (\frac{th_1^3}{12})$ and $I_2 = (\frac{th_2^3}{12})$ are, respectively, the moment of area of the lower and upper layers, and $F_1 = \epsilon_1 E_1 h_1 t$ and $F_2 = \epsilon_2 E_2 h_2 t$ are the forces in each layer. Finally, on the interface where the layers are glued together, the total strain must be equal so that

$$\epsilon_1^* + F_1/E_1 h_1 t + k_0 h_1/2 = k_0 h_2/2 + F_2/E_2 h_2 t + \epsilon_2^*$$

Solving the above system of equations for $\epsilon_1, \epsilon_2, k_0$ yields (*29*)

$$k_0 = \frac{6(\epsilon_2^* - \epsilon_1^*)(1+m)^2}{(h_1+h_2)(3(1+m)^2 + (1+mn)(m^2 + \frac{1}{mn}))} \tag{2}$$

where $m = h_1/h_2$ and $n = E_1/E_2$. We see that the curvature is proportional to the difference in the strain between the two strips and inversely proportional to the thickness of the composite.

Overwinding in the limit of infinite bending stiffness

Overwinding behavior can be intuitively understood in the limit of infinite bending stiffness relative to twisting stiffness by considering the simple case of a single helix with N turns, pitch p and radius r (Fig. S4A). This helix has uniform curvature k_0 and twist w_0 given by

$$\begin{aligned} k_0 &= \frac{r}{(r^2 + (p/2\pi)^2)} \\ w_0 &= \frac{p/2\pi}{(r^2 + (p/2\pi)^2)} \end{aligned}$$

The arclength S of this helix is related to the pitch, radius, and number of turns by $S = N\sqrt{(2\pi r)^2 + p^2}$ and its axial length L is given by $L = Np$. If this initial helix is slightly

deformed to increase its axial length from L to $L + \delta L$ without increasing its total arclength S (ie. without stretching), we assume that it will take on a new helical shape with new pitch $p + \delta p$, radius $r + \delta r$, and number of turns $N + \delta N$. If the number of helical turns is held fixed by extending the helix with both ends clamped, then $\delta N = 0$. In this case, the axial deformation δL can be accommodated by changing the pitch and radius to reduce the curvature to $k_0 - \delta k$, ie. by flattening out the helix (Fig. S4B).

However, in the limit of infinite bending stiffness relative to twisting stiffness, the helix curvature cannot change, so $\delta k = 0$. In this case, the axial deformation δL can still be achieved by allowing one end of the helix to rotate, increasing the number of turns by δN. In this case, the pitch and radius both change so as to maintain constant curvature k_0, and the number of turns increases correspondingly in order to accommodate the total helix arclength S given the new pitch and radius (Fig. S4C). This increase in the number of turns is precisely what occurs in the experimentally observed overwinding.

Condition for overwinding in a composite rod with finite bending stiffness

For helical filaments with finite bending and twisting stiffness, the effect of overwinding can again be predicted for the simple case of a single helix, following Love (*24*), which we include here for completeness.

Again we consider an initial helix with pitch p, radius r, and arclength S, but now the helix has finite bending stiffness B and twisting stiffness C. A helix with pitch p and radius r is equivalently defined by its pitch angle $\alpha = \arctan(p/2\pi r)$, shown in Fig. S4. In terms of this pitch angle and the arclength, the axial length of the helix is $L = S\sin(\alpha)$. The helix can be

described in cylindrical coordinates as

$$\begin{aligned} r(s) &= r \\ \theta(s) &= s\cos(\alpha)/r \\ z(s) &= s\sin(\alpha) \end{aligned}$$

Here the radial coordinate is a constant r, the angular coordinate θ varies from 0 to $\vartheta = S\cos\alpha/r$ at the other end, the vertical coordinate varies from 0 at one end to L at the other, and $N = \vartheta/2\pi$ is the total number of turns in the helix.

We now consider small deformations of the helix due to a force F and torque τ applied at both ends. In response to these, the helix will take on a new equilibrium shape, which we assume is a helix with the same arclength S, but new pitch angle $\alpha + \delta\alpha$ and radius $r + \delta r$. The new shape is determined by the equations of mechanical equilibrium for force and torque:

$$\begin{aligned} F &= \frac{1}{Sr^2}\left[\delta L(C\cos^2\alpha + B\sin^2\alpha) + 2\pi r\ \delta N(C-B)\sin\alpha\cos\alpha\right] \\ \tau &= \frac{1}{Sr}\left[\delta L(C-B)\sin\alpha\cos\alpha + 2\pi r\ \delta N(C\sin^2\alpha + B\cos^2\alpha)\right] \end{aligned}$$

where δN is the change in the total number of turns. Negative δN indicates unwinding, while positive δN corresponds to overwinding. In order to determine whether overwinding occurs when the helix is extended to length $L + \delta L$ under only an applied axial force, we set the applied torque $\tau = 0$ and solve for δN and δL in terms of F, l, r, B, and C. With two equations and two unknowns, we obtain the relations given in (*24*):

$$\begin{aligned} \delta L &= Sr^2\left(\frac{\sin^2\alpha}{B} + \frac{\cos^2\alpha}{C}\right)F \\ \delta N &= \frac{Sr}{2\pi}\sin\alpha\cos\alpha\left(\frac{1}{C} - \frac{1}{B}\right)F \end{aligned}$$

Since the helix pitch angle α is between 0 and $\pi/2$, the factor of $\sin\alpha\cos\alpha$ is always positive. Thus, this prediction for small deformations shows that the change in number of turns is positive

if the bending stiffness B is greater than the twisting stiffness C, and negative if $B < C$, consistent with our observations of overwinding in cucumber tendrils and numerical simulations. We note that since this linearized prediction assumes small changes in shape, it cannot quantitatively predict the eventual unwinding that is observed in the numerical simulations and the experiments. Nevertheless, this simple calculation correctly predicts the qualitative behavior observed for small extensions.

Section 3: Movie Captions

Movie S1: Time-lapse movies of tendril searching for a support and coiling

Movie S2: Drying and rehydrating a fiber ribbon

Movie S3: Drying and rehydrating a whole tendril

Movie S4: Unwinding of a physical model

Movie S5: Overwinding of a fiber ribbon

Movie S6: Overwinding in a physical model with ribbon on inside and wire on outside

Movie S7: Unwinding of a numerical filament

Movie S8: Overwinding of a numerical filament

Movie S9: Unwinding of a young cucumber tendril

Movie S10: Overwinding of an old cucumber tendril

Movie S11: Overwinding of a passiflora tendril

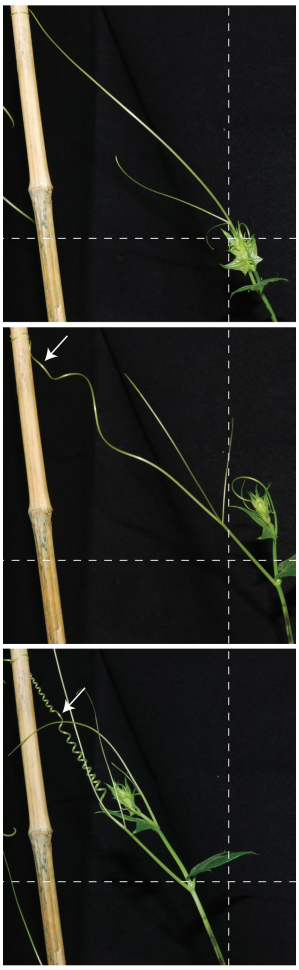

Figure S1: **Tendril climbing via helical coiling.** Cross-hairs mark the initial position of the shoot apex and highlight how tendril coiling winches the plant upward toward the support. Top: The tip of the tendril initially wraps around and attaches to the supporting rod (Time = 0). Middle: A helical perversion (arrow) initiates in the suspended tendril (Time = 120 minutes). Bottom: The tendril shortens axially by coiling into a pair of helices with opposite handedness connected by a helical perversion (Time = 390 minutes).

Figure S2: **Extracted tendril fiber ribbon cut lengthwise.** The same fiber ribbon is progressively cut lengthwise to yield narrower and narrower strips that retained the original shape. Arrows indicate helical perversion in all panels. Left: The intact fiber ribbon. Middle: Resulting fiber ribbon from one lengthwise cut. Right: The fiber ribbon from the middle panel is cut lengthwise again, yielding an even narrower ribbon with the same shape.

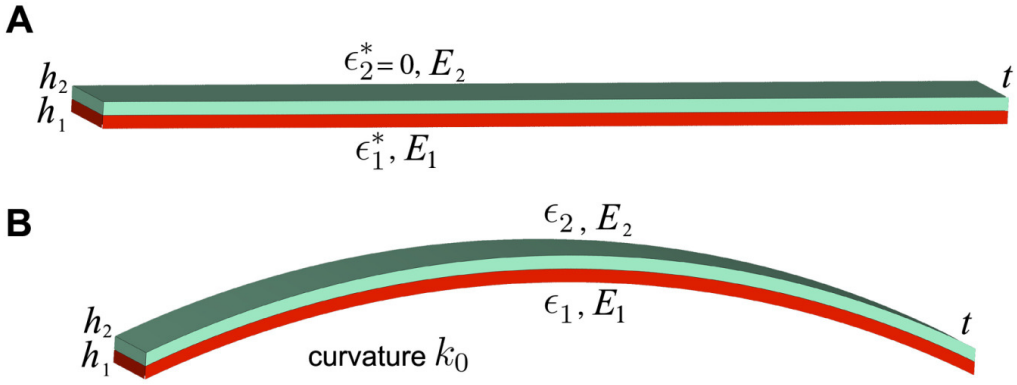

Figure S3: **Prestrain in a ribbon bilayer causes curvature.** (A) Two elastic ribbons of equal width t and heights h_1 (lower red) and h_2 (upper blue) are combined to make a bilayer ribbon. The lower layer is stretched to a strain value of ϵ_1^* and held in tension, while the upper layer is not stretched, so that $\epsilon_2^* = 0$. (B) When tension is released on the bilayer ribbon, it relaxes to its equilibrium configuration with strains ϵ_1 and ϵ_2 and curvature k_0.

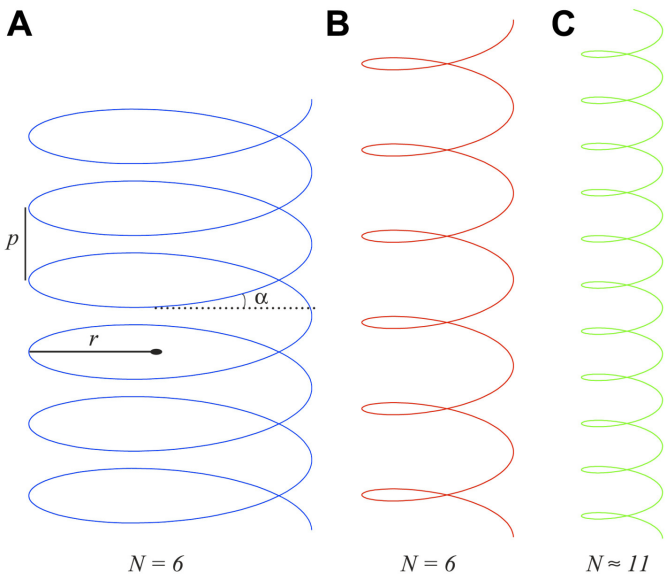

Figure S4: **Intuitive geometric explanation of overwinding in the limit of infinite bending stiffness.** (A) A helix with pitch p, radius r, pitch angle $\alpha = \arctan(p/2\pi r)$ and axial length L. (B) A deformed helix with increased axial length $L + \delta L$, achieved by maintaining a constant number of helical turns (ie. enforcing no unwinding or overwinding). (C) A deformed helix with increased axial length achieved in the limit of infinite bending stiffness by maintaining constant curvature k.

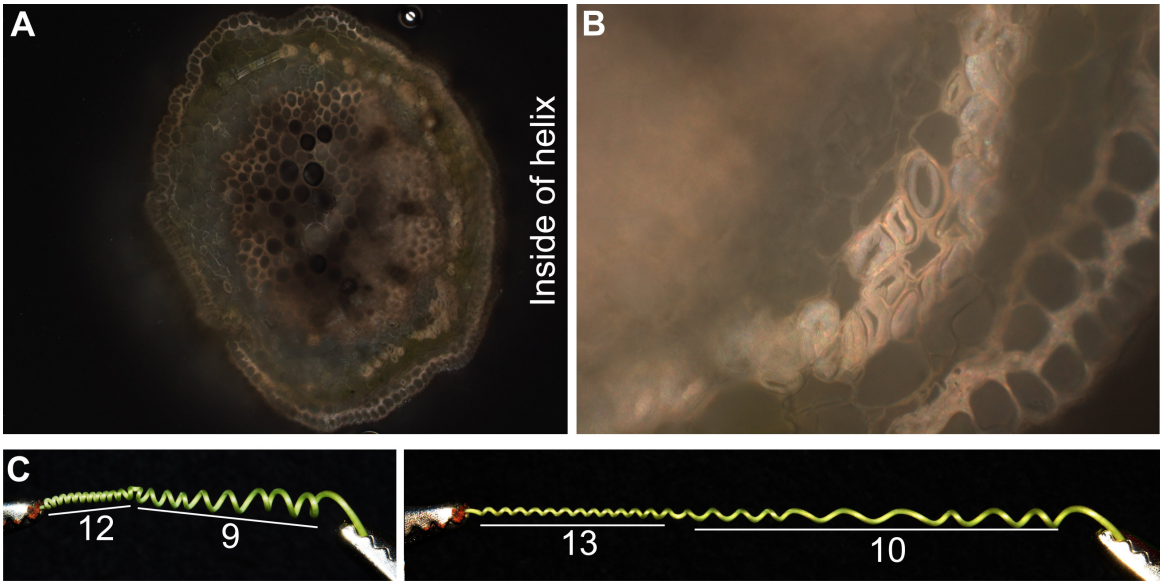

Figure S5: **Passiflora tendril anatomy and overwinding behavior.** (A) Cross section of coiled *Passiflora sp.* tendril. Gelatinous fiber (g-fiber) cells are present on the ventral side of the tendril, ie. on the inside of the helix. (B) Magnified view of g-fiber cells. Artifactual detachment of the gelatinous fiber from the secondary wall, as seen in panel B has been shown to be a distinctive characteristic of g-fiber cells (*17, 26*). (C) A coiled *Passiflora sp.* is shown in its relaxed configuration. When tension is applied, the tendril overwinds and adds additional turns on both sides of the helical perversion.

References and Notes

1. A. Gray, *Structural Botany: or Organography on the Basis of Morphology; To Which Is Added the Principles of Taxonomy and Phytography, and a Glossary of Botanical Terms* (Ivison, Blakeman, Taylor, New York, 1880).

2. H. v. Mohl, *Principles of the Anatomy and Physiology of the Vegetable Cell* (John Van Voorst, London, 1852).

3. C. Darwin, *On the Movements and Habits of Climbing Plants* (John Murray, London, 1865).

4. R. Dastur, G. Kapadia, *Ann. Bot. (Lond.)* **45**, 279 (1931).

5. M. Jaffe, A. Galston, The physiology of tendrils. *Annu. Rev. Plant Physiol.* **19**, 417 (1968). doi:10.1146/annurev.pp.19.060168.002221

6. A. Goriely, M. Tabor, Spontaneous helix hand reversal and tendril perversion in climbing plants. *Phys. Rev. Lett.* **80**, 1564 (1998). doi:10.1103/PhysRevLett.80.1564

7. H. Lisk, Cellular structure of tendrils. *Bot. Gaz.* **78**, 85 (1924). doi:10.1086/333357

8. D. T. MacDougal, *Annal. Bot.* **os-10**, 373 (1896).

9. S. Isnard, W. K. Silk, Moving with climbing plants from Charles Darwin's time into the 21st century. *Am. J. Bot.* **96**, 1205 (2009). doi:10.3732/ajb.0900045 Medline

10. B. F. Wilson, R. R. Archer, Reaction wood: Induction and mechanical action. *Annu. Rev. Plant Physiol.* **28**, 23 (1977). doi:10.1146/annurev.pp.28.060177.000323

11. W. Silk, R. Erickson, Kinematics of hypocotyl curvature. *Am. J. Bot.* **65**, 310 (1978). doi:10.2307/2442271

12. J. L. Scher, N. M. Holbrook, W. K. Silk, Temporal and spatial patterns of twining force and lignification in stems of Ipomoea purpurea. *Planta* **213**, 192 (2001). doi:10.1007/s004250000503 Medline

13. S. Isnard, A. R. Cobb, N. M. Holbrook, M. Zwieniecki, J. Dumais, Tensioning the helix: A mechanism for force generation in twining plants. *Proc. Biol. Sci.* **276**, 2643 (2009). doi:10.1098/rspb.2009.0380 Medline

14. U. Nath, B. C. W. Crawford, R. Carpenter, E. Coen, Genetic control of surface curvature. *Science* **299**, 1404 (2003). doi:10.1126/science.1079354 Medline

15. J. B. Keller, *Lect. Math Life Sci.* **13**, 257 (1980).

16. T. McMillen, A. Goriely, Tendril perversion in intrinsically curved rods. *J. Nonlinear Sci.* **12**, 241 (2002). doi:10.1007/s00332-002-0493-1

17. C. G. Meloche, J. P. Knox, K. C. Vaughn, A cortical band of gelatinous fibers causes the coiling of redvine tendrils: A model based upon cytochemical and immunocytochemical studies. *Planta* **225**, 485 (2007). doi:10.1007/s00425-006-0363-4 Medline

18. A. J. Bowling, K. C. Vaughn, Gelatinous fibers are widespread in coiling tendrils and twining vines. *Am. J. Bot.* **96**, 719 (2009). doi:10.3732/ajb.0800373 Medline

19. L. Goswami *et al*., Stress generation in the tension wood of poplar is based on the lateral swelling power of the g-layer. *Plant J.* **56**, 531 (2008). doi:10.1111/j.1365-313X.2008.03617.x Medline

20. Materials and methods are available as supplementary materials on *Science* Online.

21. Z. Chen, C. Majidi, D. J. Srolovitz, M. Haataja, Tunable helical ribbons. *Appl. Phys. Lett.* **98**, 011906 (2011). doi:10.1063/1.3530441

22. S. Armon, E. Efrati, R. Kupferman, E. Sharon, Geometry and mechanics in the opening of chiral seed pods. *Science* **333**, 1726 (2011). doi:10.1126/science.1203874 Medline

23. T. Savin *et al*., On the growth and form of the gut. *Nature* **476**, 57 (2011). doi:10.1038/nature10277 Medline

24. A. Love, *A Treatise on the Mathematical Theory of Elasticity* (Courier Dover Publications, Mineola, NY, 1944).

25. P. F. Stevens, Angiosperm phylogeny website, www.mobot.org/MOBOT/Research/APweb/welcome.html (2008).

26. B. Clair, B. Thibaut, J. Sugiyama, On the detachment of the gelatinous layer in tension wood fiber. *J. Wood Sci.* **51**, 218 (2005). doi:10.1007/s10086-004-0648-9

27. M. Bergou, M. Wardetzky, S. Robinson, B. Audoly, E. Grinspun, Discrete elastic rods. *ACM Trans. Graph.* **27**, 1 (2008). doi:10.1145/1360612.1360662

28. S. S. Antman, Nonlinear problems of elasticity (Springer, 2005), second edn.

29. S. Timoshenko, Analysis of bi-metal thermostats. *J. Opt. Soc. Am.* **11**, 233 (1925). doi:10.1364/JOSA.11.000233